Ferrite Formation Dynamics and Microstructure Due to Inclusion Engineering in Low-Alloy Steels by Ti$_2$O$_3$ and TiN Addition

WANGZHONG MU, HIROYUKI SHIBATA, PETER HEDSTRÖM, PÄR GÖRAN JÖNSSON, and KEIJI NAKAJIMA

The dynamics of intragranular ferrite (IGF) formation in inclusion engineered steels with either Ti$_2$O$_3$ or TiN addition were investigated using *in situ* high temperature confocal laser scanning microscopy. Furthermore, the chemical composition of the inclusions and the final microstructure after continuous cooling transformation was investigated using electron probe microanalysis and electron backscatter diffraction, respectively. It was found that there is a significant effect of the chemical composition of the inclusions, the cooling rate, and the prior austenite grain size on the phase fractions and the starting temperatures of IGF and grain boundary ferrite (GBF). The fraction of IGF is larger in the steel with Ti$_2$O$_3$ addition compared to the steel with TiN addition after the same thermal cycle has been imposed. The reason for this difference is the higher potency of the TiO$_x$ phase as nucleation sites for IGF formation compared to the TiN phase, which was supported by calculations using classical nucleation theory. The IGF fraction increases with increasing prior austenite grain size, while the fraction of IGF in both steels was the highest for the intermediate cooling rate of 70 °C/min, since competing phase transformations were avoided, the structure of the IGF was though refined with increasing cooling rate. Finally, regarding the starting temperatures of IGF and GBF, they decrease with increasing cooling rate and the starting temperature of GBF decreases with increasing grain size, while the starting temperature of IGF remains constant irrespective of grain size.

I. INTRODUCTION

NON-METALLIC inclusions in steels are generally considered to be detrimental for the mechanical properties. However, certain non-metallic inclusions, such as Ti-oxide and TiN, are recognized to serve as potent nucleation sites for the formation of intragranular ferrite (IGF) in low-alloy steels. This preferential formation of IGF, a desirable microstructure, reduces the amount of grain boundary ferrite (GBF) and, hence, improves the toughness of the steel. There are two concepts associated with this principle. Firstly, "oxide metallurgy"[1] describes the utilization of fine oxide inclusions to improve the final steel product quality. Secondly, "inclusion engineering" utilizes the same phenomenon but herein all kinds of inclusions, including nitrides, oxides, and sulfides, are considered.[2] In order to apply the concept of inclusion engineering for the microstructure control, a specially designed master alloy containing fine inclusions[3] have been suggested to be added into the steel. Moreover, different additives with metallic Ti and TiO$_2$ powders,[4] Ti$_2$O$_3$ and TiN powders[5,6] have been added into the liquid steel directly to control the microstructure of the steels.

To fully benefit from oxide metallurgy and inclusion engineering, it is necessary to have a detailed knowledge of the inclusion characteristics as well as the dynamic phase transformation behavior during the austenite decomposition process. *In situ* confocal laser scanning microscope (CLSM) is capable of such measurements and it can be utilized for real-time dynamic observations of IGF and GBF formation. CLSM has been frequently used to study the formation of IGF from various inclusions such as MnAl$_2$O$_4$,[7] Ce-containing,[8] Mg-containing,[9] Al$_2$O$_3$ + MnS + TiN,[10] and Ti-rich[11,12] inclusions. Kikuchi *et al.* have studied the austenite grain growth and austenite decomposition in low-carbon high-manganese steels deoxidized by Ti or Al.[13] In particular, the effect of the prior austenite grain size on the area fraction of IGF, the starting temperatures of IGF ($T_{\mathrm{IGF,s}}$) and GBF ($T_{\mathrm{GBF,s}}$) formation and

WANGZHONG MU, formerly Ph.D. Candidate with the Department of Materials Science and Engineering, KTH Royal Institute of Technology, Brinellvägen 23, Stockholm, 10044 Sweden, is now Postdoctoral Fellow at the Department of Materials Science and Engineering, McMaster Steel Research Center, McMaster University, 1280 Main Street West, Hamilton, ON, L8S 4L7, Canada. Contact e-mail: muw@mcmaster.ca PETER HEDSTRÖM, Assistant Professor, and PÄR GÖRAN JÖNSSON and KEIJI NAKAJIMA, Professors, are with the Department of Materials Science and Engineering, KTH Royal Institute of Technology, Brinellvägen 23, 10044, Stockholm, Sweden. Contact e-mail: keiji@kth.se HIROYUKI SHIBATA, Professor, is with the Institute of Multidisciplinary Research for Advanced Materials, Tohoku University, 2-1-1 Katahira, Aoba-ku, Sendai, Miyagi, 980-8577 Japan.

ferrite formation in rapidly cooled weld metal have been successfully studied by CLSM.[11,12,14] However, CLSM can provide only part of the necessary information and complementary experimental information is required. Electron backscatter diffraction (EBSD) has been frequently used to investigate the final microstructural characteristics,[15–18] and there are a few reports where EBSD has been combined with CLSM to investigate austenite decomposition in steels. For instance using this approach, Wan et al.[10] investigated the formation of acicular ferrite and bainite in a simulated coarse-grained heat-affected zone and Phelan and coworkers investigated the formation of Widmanstätten ferrite in a low-carbon steel grade.[19,20]

There are, though, few quantitative dynamic studies of IGF formation where the effect of the composition of the inclusions and the cooling rate on the final microstructure, including the phase fractions, has been comprehensively investigated. The purpose of the present work is therefore to perform a study of the formation of IGF and GBF in inclusion engineered steels with Ti_2O_3 or TiN addition. The investigation is performed using a combination of experimental tools such as In situ CLSM, EBSD, and EPMA. The effect of the inclusions on the formation of IGF and GBF is elucidated, and the effect of the cooling rate and the prior austenite grain size on the formation of IGF and GBF is also discussed. Furthermore, the experimental results are complemented by calculations of thermodynamic driving forces and nucleation barriers.

II. METHODOLOGY

A. Experimental Methods

The compositions of the investigated alloys are presented in Table I, and for more details about the alloy preparation, the reader is referred to Mu et al.[5,6] From hereon, the steels with Ti_2O_3 and TiN addition are called alloy A and B, respectively. The steel specimens were prepared by cutting of small cylindrical pieces ($\Phi 4.1$ mm × 1 mm thickness) and subsequently polishing one flat side using abrasive papers (80#, 220#, 800#, and 1200#) and finally by alumina suspension (1 μm). Thereafter, the specimen was placed in a high-purity alumina crucible ($\Phi 5.5$ mm O.D × $\Phi 4.5$ mm I.D × 5 mm height) and mounted in the hot-stage CLSM equipment. The details of the CLSM setup can be found in References 21 through 24.

The specimen was heated to a temperature of 1673 K (1400 °C) using a heating rate of 20 °C/min, and thereafter directly cooled to a temperature of 673 K (400 °C) without holding. The cooling rate from 1223 K

to 673 K (950 °C to 400 °C) was controlled to be constant at 3.6 and 70 °C/min, and the third cooling rate was in average 678 °C/min. These thermal cycles are presented in Figure 1. In addition, to control the prior austenite grain size, the specimens were also heated up to temperatures of 1473 K, 1523 K, 1573 K, and 1673 K (1200 °C, 1250 °C, 1300 °C, and 1400 °C), and, moreover, the holding time at 1673 K (1400 °C) was varied from 0 to 5 and 10 minutes. The effect of the holding conditions on the grain size is shown in Figure 2.

Pure Ar gas (purity > 99.9999 pct), further cleaned by passing it through a heated Ti column at 773 K (500 °C), was used as the furnace atmosphere. In addition, a Ti-foil was wrapped around the upper part of the alumina crucible to prevent oxidation of the specimen surface. The temperature of the crucible and the specimen surface was measured using PtRh30 pct-PtRh6 pct (type B) thermocouples, attached to the bottom of the crucible and welded to the surface of the specimen, respectively. The measured temperature
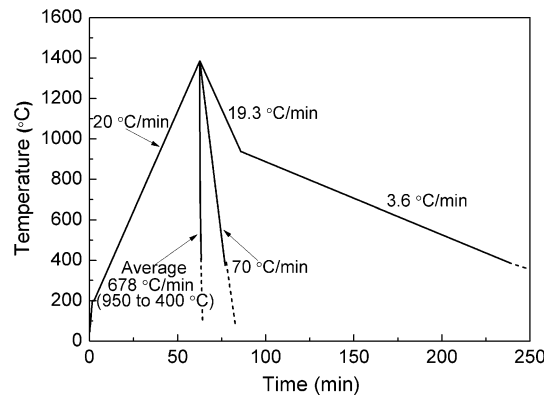

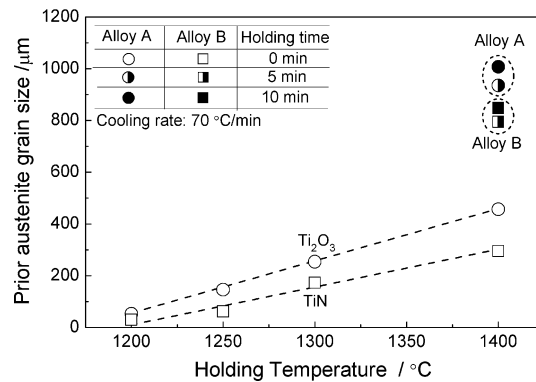Fig. 1—Thermal cycles employed in the present work.

Fig. 2—Prior austenite grain size in alloy A and alloy B at different holding temperatures.

Table I. Chemical Compositions of Steels with Ti_2O_3 and TiN Additions (Mass Percent)

Sample	C	Si	Mn	Al	Ti	S	N	O	Fe
Alloy A	0.223	0.24	1.02	0.002	0.013	0.009	0.017	0.0072	bal.
Alloy B	0.227	0.38	0.91	<0.002	0.008	0.009	0.029	0.0071	bal.

* Alloy A: steel sample with Ti_2O_3 addition; Alloy B: steel sample with TiN addition.

difference between these two positions was on average 13 K (13 °C) between 1023 K and 923 K (750 °C and 650 °C) for a cooling rate of 3.6 °C/min, 26 K (26 °C) between 1023 K and 923 K (750 °C and 650 °C) for a cooling rate of 70 °C/min, and 43 K (43 °C) between 873 K and 823 K (600 °C and 550 °C) for a cooling rate of 678 °C/min. The measured temperature differences show that small temperature gradients could exist in the samples during rapid cooling, but this effect is deemed small and the measured surface temperature is used from hereon.

Selected CLSM micrographs and the commercial image analysis software WinROOF® were used to measure the fraction of IGF and GBF on a total area of about 0.69 mm^2 per sample. The prior austenite grain size was also evaluated using WinROOF® and the grain size was taken as an average value of 10 typical grains. The reason for choosing only 10 grains was that only a few complete grains were found in one section of the specimen due to the coarse grain size in several of the samples in the present work. The average grain size estimated based on 10 grains was also compared to the average value estimated from 20 grains when the grain size was less than 468 μm, and the estimations were in good agreement.

The chemical composition of the inclusions was measured using EPMA (JEOL JXA-8200 WD/ED). For light-element analysis, i.e., O and N, WDS was used. The concentration of each element was calibrated using standard samples (Fe$_2$O$_3$, MnO, TiO$_2$, AlN, Si, FeS$_2$) and a similar procedure as in Reference 25 prior analysis. The microstructure was characterized using EBSD measurements on the same specimens that were used for the *In situ* observations, and the step sizes used were 0.8 and 0.1 μm. The EBSD detectors Nordlys Nano (Oxford Instruments) and e-FLASH HR (Bruker) in a field emission scanning electron microscope (FE-SEM) (JEOL JSM-7800F) was used. The microscope was operated at an acceleration voltage of 15 kV and the softwares HKL Channel 5 (Oxford Instruments) and Quantax (Bruker) were used during the EBSD analysis.

B. *Calculation Methods*

The relation between the normalized energy barrier for IGF nucleation, $\Delta G_{het}^*/\Delta G_{hom}^*$ and the inclusion size can be expressed as in Eq. [1].[26] θ represents the angle between the surface of the inclusion and the ferrite phase, as illustrated in Figure 3. $\cos\theta$ is calculated by Eq. [2],[26] where $\sigma_{I\alpha}$ is the interfacial energy between the inclusion and the ferrite phase, and where $\sigma_{I\gamma}$ is the interfacial energy between the inclusion and the austenite phase, whereas $\sigma_{\gamma\alpha}$ is the interfacial energy between the austenite and the ferrite phases. Furthermore, u and x are defined to simplify the expression of $f(\theta,x)$ as shown in Eqs. [3] and [4],[26] where R is the radius of the inclusion phase, and r^* is the critical radius of the IGF phase. r^* is calculated according to Eq. [5], where ΔG_v is the driving force for ferrite formation, which is here calculated by Thermo-Calc[27] and the TCFE7 database.[28]
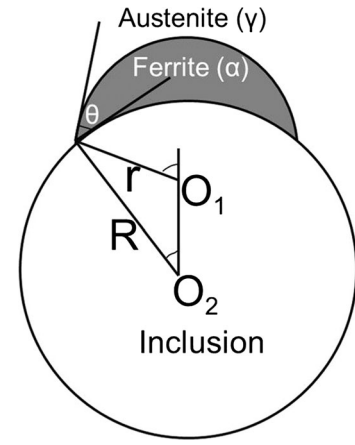

Fig. 3—Schematic of IGF nucleation on the surface of a spherical inclusion.

$$f(\theta, x) = \Delta G_{het}^*/\Delta G_{hom}^* = \frac{1}{2} + \frac{1}{2}\left(\frac{1 - x\cos\theta}{u}\right)^3$$
$$+ \frac{x^3}{2}\left(2 - 3\left(\frac{x - \cos\theta}{u}\right) + \left(\frac{x - \cos\theta}{u}\right)^3\right) \quad [1]$$
$$+ \frac{3x^2\cos\theta}{2}\left(\frac{x - \cos\theta}{u} - 1\right)$$

$$\cos\theta = (\sigma_{I\gamma} - \sigma_{I\alpha})/\sigma_{\gamma\alpha} \quad [2]$$

$$u = (1 + x^2 - 2x\cos\theta)^{1/2} \quad [3]$$

$$x = R/r^* = R/(2\sigma_{\gamma\alpha}/\Delta G_v) \quad [4]$$

$$r^* = 2\sigma_{\gamma\alpha}/\Delta G_v. \quad [5]$$

The interfacial energy between the inclusion and the austenite/ferrite phase constitute of both a chemical interfacial energy and a misfit strain energy,[29–32] based on Eqs. [6] and [7].

$$\sigma_{I\gamma} = \sigma_{I\gamma,c} + \sigma_{I\gamma,s} \quad [6]$$

$$\sigma_{I\alpha} = \sigma_{I\alpha,c} + \sigma_{I\alpha,s} \quad [7]$$

$\sigma_{I\gamma,c}$ and $\sigma_{I\alpha,c}$ are the chemical interfacial energy between inclusion and austenite (γ)/ferrite (α), whereas $\sigma_{I\gamma,s}$ and $\sigma_{I\alpha,s}$ are the misfit strain energy between inclusion and austenite (γ)/ferrite (α). The values reported by Yang et al.[33] were used for the chemical interfacial energy between inclusion and austenite (γ)/ferrite (α), whereas the misfit strain energy was calculated based on Eqs. [8] through [12] for a semi-coherent interface.[34] The physical parameters for these calculations were taken from the literature[35–41] and are summarized in Table II. The calculated values of the misfit strain energy between inclusions and austenite/ferrite are shown in Table III, and the values range from 0.379 to 0.810 J/m^2. This is in good agreement with a previous study[42] where the misfit strain energy

Table II. Physical Parameters for the Calculation of Misfit Strain Energy

Symbol	Explanation	Value	Ref.
$\delta_{\text{TiN}/\gamma}$	misfit between TiN and austenite	16.96 pct	Pan et al.[35]
$\delta_{\text{TiN}/\alpha}$	misfit between TiN and ferrite	4.6 pct	Mills et al.[36]
$\delta_{\text{TiO}/\gamma}$	misfit between TiO and austenite	15.79 pct	Pan et al.[35]
$\delta_{\text{TiO}/\alpha}$	misfit between TiO and ferrite	3.0 pct	Mills et al.[36]
a_{TiN}	lattice parameter of TiN	0.424 nm	Mills et al.[36]
a_{TiO}	lattice parameter of TiO	0.418 nm	Mills et al.[36]
a_γ	lattice parameter of austenite	0.359 nm	Galasso[37]
a_α	lattice parameter of ferrite	0.286 nm	Galasso[37]
μ_{TiN}	shear modulus of TiN	231 GPa	Zhang et al.[38]
μ_{TiO}	shear modulus of TiO	241.54 GPa	Ciftci et al.[39]
μ_γ	shear modulus of austenite	81.6 GPa	Zhang et al.[38]
μ_α	shear modulus of ferrite	42.3 GPa	Fukuhara and Sampei[40]
ν_{TiN}	Poisson's ratio of TiN	0.300	Perry[41]
ν_{TiO}	Poisson's ratio of TiO	0.232	Ciftci et al.[38]
ν_γ	Poisson's ratio of austenite	0.350	Fukuhara and Sampei[40]
ν_α	Poisson's ratio of ferrite	0.290	Fukuhara and Sampei[40]

was calculated to be from 0.2 to 0.8 J/m². Hence, the calculated misfit strain energies are reasonable.

$$\sigma_s = \frac{\mu c}{4\pi^2}\left(1 + \beta - \left(1+\beta^2\right)^{1/2} - \beta\ln\left(2\beta\left(1+\beta^2\right)^{1/2} - 2\beta^2\right)\right)$$
[8]

$$\mu = \frac{\mu_m + \mu_I}{2},$$
[9]

$$c = \frac{a_m + a_I}{2},$$
[10]

$$\beta = \frac{2\pi\delta_{Im}\lambda}{\mu},$$
[11]

$$\lambda = \frac{1}{\left(\frac{1-\nu_m}{\mu_m} + \frac{1-\nu_I}{\mu_I}\right)}$$
[12]

μ is the average of the shear modulus of the two phases; the subscript I stands for the inclusion phase, i.e., TiO or TiN; m stands for the metal phase, which is austenite (γ) and ferrite (α); c is the average of the lattice parameter of the inclusion phase and the metal phase; β is calculated by the misfit between the metal phase and the inclusion phase (δ_{Im}), shear modulus (μ), and Poisson's ratio (ν).

Equations [13] through [14] describe the method for calculating the GBF nucleation from grain boundaries[43].

$$f'(\theta) = \frac{\Delta G_{het}^*}{\Delta G_{hom}^*} = \frac{1}{4}(2 + \cos\phi)(1 - \cos\phi)^2$$
[13]

$$\cos\phi = \sigma_{\gamma\gamma}/2\sigma_{\gamma\alpha}$$
[14]

$\sigma_{\gamma\gamma}$ is the interfacial energy of austenitic interfaces and $\cos\varphi$ is calculated by the ratio of $\sigma_{\gamma\gamma}/\sigma_{\gamma\alpha}$.

III. RESULTS

A. Chemical Composition of Inclusions

Figure 4(a) shows that Ti-oxide, from hereon referred to as TiO_x, is the main phase in both the core and the surface of the inclusions in the steel with Ti_2O_3 addition (alloy A). Moreover, different parts of the inclusion were measured by EPMA point analysis. A typical location of a measurement is shown in Figure 5 and the results are shown in Table IV. It was found that the atomic ratio of O/Ti, x, is between 1.55 and 1.69. Besides TiO_x, MnS inclusions and small amounts of Mn-Al-Si-O oxide, previously reported to be a glassy amorphous Mn-Al-Si-O phase,[44] are randomly distributed outside the corners of the TiO_x core. These typical inclusions in alloy A are designated to be a TiO_x + MnS inclusion. In addition, the Al content is 1.14 to 1.58 at. pct in the oxide phase, which is much lower than the Ti content. Also, the Mn content is 0.81 to 3.61 at. pct and the S content is 0.55 to 4.29 at. pct. in the oxide phase. Note, that a typical spinel type inclusion, such as Ti-Al-O or Ti-Mn-O, has not been found in alloy A.

Figure 4(b) shows the elemental distribution maps for a typical inclusion in the steel with TiN addition (alloy B). The core part is a Mn-Al-Si-Ti-O phase and the EPMA analysis shows that the chemical composition of the glassy amorphous Mn-Al-Si-Ti-O phase is 13.4 at. pct Si, 12.4 at. pct Al, 10.5 at. pct Mn, 2.5 at. pct Ti, and 59.9 at. pct O. Moreover, TiN is found to precipitate on the surface of the Mn-Al-Si-Ti-O phase. This outer layer of TiN is considered to be the nucleation site for IGF formation. The atomic ratios of N to Ti range from 0.8 to 1.3 and; moreover, MnS was found to precipitate randomly at the corners of the core of the Mn-Al-Si-Ti-O phase. These typical inclusions in alloy B are designated to be a TiN + MnS + Mn-Al-Si-Ti-O inclusion.

Table III.   Physical Parameters for the Calculation of Normalized Energy Barrier of IGF and GBF Nucleation

Symbol	Explanation	Value		Ref./Present work
$\sigma_{I\gamma,c}$	chemical interfacial energy between inclusion and austenite	TiO	0.839 J/m^2	Yang et al.[33]
		TiN	0.636 J/m^2	Yang et al.[33]
$\sigma_{I\alpha,c}$	chemical interfacial energy between inclusion and ferrite	TiO	0.627 J/m^2	Yang et al.[33]
		TiN	0.439 J/m^2	Yang et al.[33]
$\sigma_{I\gamma,s}$	misfit strain energy between inclusion and austenite	TiO	0.773 J/m^2	present work
		TiN	0.810 J/m^2	present work
$\sigma_{I\alpha,s}$	misfit strain energy between inclusion and austenite	TiO	0.379 J/m^2	present work
		TiN	0.502 J/m^2	present work
$\sigma_{\gamma\alpha}$	interfacial energy between austenite and ferrite	0.75 J/m^2		Ricks et al.[53]
$\sigma_{\gamma\alpha}/\sigma_{\gamma\gamma}$	ratio between $\sigma_{\gamma\alpha}$ and $\sigma_{\gamma\gamma}$	1.0		Ricks et al.[53]
		0.943		Gjostein et al.[69]
		0.72		Valck[70]
ΔG_v	driving force per volume for ferrite formation	4.26×10^7 J/m^3 [973 K (700 °C)]		present work by Thermo-Calc.

B. *Prior Austenite Grain Size*

Figure 2 shows the relationship between the prior austenite grain size and the holding conditions of the steels with either Ti$_2$O$_3$ or TiN addition. The grain size in Figure 2 was measured for the steel that was cooled at 70 °C/min but it was also confirmed that the grain size was constant within ±30 μm regardless of the cooling rate. The prior austenite grain size increases with increasing holding temperature from 1473 K to 1673 K (1200 °C to 1400 °C) and with increasing holding time from 0 to 10 minutes. Moreover, the grain size in alloy A is larger than that in alloy B.

C. *Area Fraction of IGF*

Figures 6(a) and (b) show the effect of prior austenite grain size on the area fraction of IGF in the steels with Ti$_2$O$_3$ and TiN additions. Furthermore, the relationship between the cooling rate and the phase fractions are plotted in Figures 7(a) and (b) for the steel samples that were heated to 1673 K (1400 °C) without holding. It can be seen that when the cooling rate and the grain size are kept constant, the area fraction of IGF is larger in alloy A than in alloy B. Moreover, the area fraction of IGF increases with increasing prior austenite grain size and with increasing cooling rate from 3.6 to 70 °C/min, a tendency that was observed for both steel alloys.

D. *Starting Temperature of IGF and GBF Formation*

Figure 8 shows typical images of the initial formation of GBF and IGF with different grain sizes in alloy A, as observed by CLSM. It is clear that $T_{GBF,s}$ in the steel with a relatively small grain size is higher than that in the steels with a coarse grain size, while $T_{IGF,s}$ is almost constant regardless of the grain size. CLSM micrographs of IGF and GBF formation for different cooling rates are shown in Figure 9. It is seen that the GBF forms at a higher temperature than the IGF does and, moreover, the values of $T_{GBF,s}$ and $T_{IGF,s}$ decrease with increasing cooling rate. The values of $T_{GBF,s}$ and $T_{IGF,s}$

for different grain sizes and treated using different cooling rates are shown in Figures 10(a) and (b). It can be seen that $T_{GBF,s}$ is lower for the steels with Ti$_2$O$_3$ addition compared to the steels with TiN addition, while $T_{IGF,s}$ is almost the same for the two alloys.

IV.   DISCUSSION

A. *Effect of the Inclusions on the IGF Formation*

As shown in Figure 6, the fraction of IGF is higher in alloy A than in alloy B. The number density of inclusions is 53.9/mm^2 in alloy A and 58.8/mm^2 in alloy B. This slight difference in number density is assumed to be negligible in the current work. The difference of the area fraction of IGF is due to the nuclei inclusions in alloy A are more effective to promote the formation of IGF than those in alloy B. Homma et al.[45] and Lee and Pan[46,47] have reported that TiO$_x$ inclusions are more potent nucleation sites for IGF formation than TiN inclusions. This has also been confirmed by Lee[48] who calculated the relative nucleation potential of IGF to GBF and demonstrated that Ti-oxide inclusions have superior nucleation potential compared to TiN inclusions. Mu et al.[7] have reported the probability of IGF nucleation at each inclusion size range using the number of inclusions where ferrite nucleates divided by the total number of inclusions. Their results show that the nucleation probability of TiO$_x$ inclusion is higher than that of TiN inclusion for each inclusion size range. Looking more in detail at the characteristics of the inclusions, previous studies have reported that a TiO phase is present on the surface of the complex TiO$_x$ particles in steels with a Ti$_2$O$_3$ addition.[49,50] A study of the interfacial structure between the TiO and the adjacent IGF in a low-carbon steel has also been reported.[51] Based on the experimental evidence, the physical properties of TiO phase were used to represent those of TiO$_x$ inclusions in the calculations of an IGF nucleation.
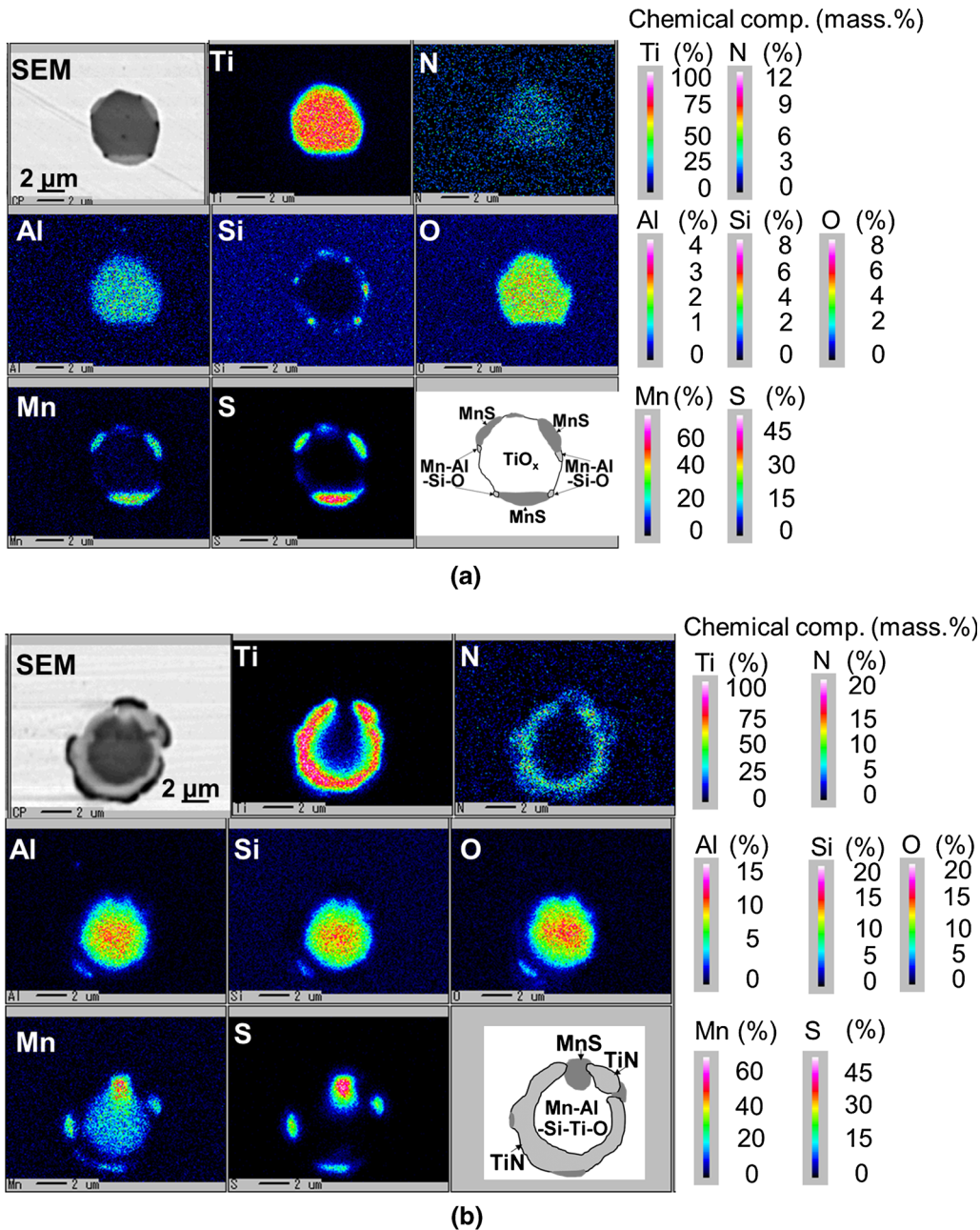
Fig. 4—Chemical maps of Ti, N, Al, Si, O, Mn, and S in inclusions, determined by EPMA, for (a) alloy A and (b) alloy B.

Several mechanisms have been suggested to cause the different potencies of inclusions toward IGF nucleation. It has been suggested that the reduction of the energy barrier for nucleation of the ferrite phase is the primary cause.[52] Furthermore, it has been stated that the energy barrier of heterogeneous nucleation normalized by homogeneous nucleation of IGF $\left(\Delta G^*_{het.}/\Delta G^*_{hom.}\right)$ continuously decreases with increasing inclusion size.[53,54] Ricks et al.[53] reported that the inclusion surfaces are always energetically less favorable than the prior austenite grain boundaries for ferrite nucleation. Their conclusions were based on classical nucleation theory[54] showing that the ferrite prefers to nucleate at the surface of the inclusions instead of at the grain boundaries when the sizes of the inclusions are larger than the critical sizes.

In this work, the normalized energy barrier of IGF formation $\left(\Delta G^*_{het.}/\Delta G^*_{hom.}\right)$ was calculated at each inclusion size. The effect of the inclusion size on the normalized energy barrier of IGF and GBF nucleation is shown in Figure 11, where (a) is plotted for the chemical interfacial energy alone, (b) is plotted for the misfit strain energy alone, and (c) shows the combined result, i.e., considering the total energy. The critical radii of TiO and TiN inclusions are in the range from 0.1 to 0.3 μm, 0.07 to 0.2 μm, and 0.03 to 0.05 μm in Figures 11(a), (b), and (c), respectively. These results predict that TiO and TiN could become effective

nucleation sites for IGF when their sizes are larger than the critical size. It is found that the actual inclusion size in the investigated steels is larger than the critical size, and thus the inclusions are large enough to become effective nucleation sites for IGF. Furthermore, the critical size of TiO is smaller than that of TiN, see Figures 11(a), (b), and (c). The fact that TiO has a higher potency to induce IGF nucleation than TiN could explain why the fraction of IGF nucleated from TiO_x is higher than that from TiN.
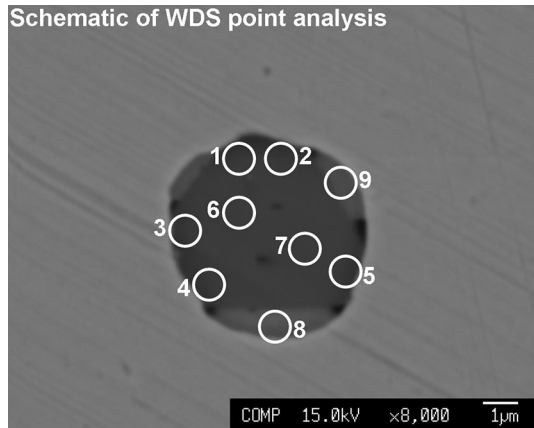
Fig. 5—Schematic locations of EPMA point analysis of a typical inclusion in alloy A.

B. *Effect of Prior Austenite Grain Size on the IGF Formation*

Figure 6 shows that the fraction of IGF is increased with increasing prior austenite grain size, and this tendency could be observed regardless of the composition of the inclusions and the cooling rate. This tendency is in agreement with previous results in steels using a cooling rate of 300 °C/min.[11] Furthermore, Liu and Olson[55] reported that the larger sized grains provide a larger physical space inside the grains for nucleation and growth of IGF, and this is considered to be the reason for the larger fraction of IGF in the steels with a larger grain size. Finally, it is noted that when the average grain size is larger than 470 μm [holding at 1673 K (1400 °C) × 0 minutes] in alloy A and larger than about 295 μm [holding at 1673 K (1400 °C) × 0 minutes] in alloy B, the area fraction of IGF only increases slightly. Therefore, since both a large area fraction of IGF and a fine grain size is desirable, the holding at 1673 K (1400 °C) for 0 minutes seems to be the preferred condition in the present work.

In Figure 10, it is noted that $T_{GBF,s}$ of alloy A is lower than that of alloy B, and the difference in the value of $T_{GBF,s}$ is due to the difference in grain size. Specifically, alloy B has an average grain size of about 295 μm, whereas alloy A has an average grain size of about 470 μm at the same holding condition of 1673 K (1400 °C) × 0 minutes, and this phenomenon is due to the pinning effect of TiN inclusions.[56] This difference in behavior can be explained in terms of nucleation

Table IV.   EPMA Point Analysis of Alloy A (Mass Percent)

	Point 1 (TiO_x, $x = 1.65$)			Point 2 (TiO_x, $x = 1.66$)			Point 3 (TiO_x, $x = 1.68$)		
	Mass pct	Atomic pct	Error pct	Mass pct	Atomic pct	Error pct	Mass pct	Atomic pct	Error pct
O	25.42	48.08	1.32	27.69	50.91	1.32	31.25	55.89	1.28
Ti	46.19	29.19	1.63	49.87	30.63	1.60	55.63	33.23	1.51
Al	1.02	1.14	2.93	1.09	1.18	2.87	1.31	1.39	2.56
Fe	12.94	7.01	1.17	10.56	5.56	1.32	7.48	3.83	1.59
N	2.84	6.13	10.23	3.01	6.31	9.90	2.06	4.21	12.47
Mn	6.55	3.61	3.23	4.75	2.54	3.89	1.57	0.81	7.18
Si	0.51	0.55	4.08	0.45	0.47	4.45	0.08	0.08	18.70
S	4.54	4.29	1.35	2.60	2.39	1.84	0.62	0.55	3.90
	Point 4 (TiO_x, $x = 1.64$)			Point 5 (TiO_x, $x = 1.54$)			Point 6 (TiO_x, $x = 1.69$)		
O	30.32	54.57	1.29	27.55	51.18	1.36	33.17	57.75	1.25
Ti	55.27	33.22	1.51	53.32	33.09	1.53	58.92	34.26	1.45
Al	1.35	1.44	2.52	1.29	1.42	2.60	1.53	1.58	2.31
Fe	7.35	3.79	1.59	11.08	5.89	1.29	2.32	1.15	2.99
N	2.17	4.45	11.21	2.64	5.60	10.51	2.14	4.25	11.70
Mn	1.87	0.98	6.47	2.77	1.50	5.18	1.85	0.94	6.53
Si	0.38	0.39	5.11	0.46	0.48	4.64	0.07	0.06	20.92
S	1.30	1.16	2.61	0.90	0.83	3.17	—	—	—
	Point 7 (TiO_x, $x = 1.69$)			Point 8 (MnS)			Point 9 (MnS)		
O	33.22	57.58	1.25	3.19	8.57	3.50	3.34	9.07	4.05
Ti	58.91	34.11	1.44	10.28	9.23	3.41	22.83	20.73	2.39
Al	1.27	1.31	2.53	0.32	0.52	6.62	0.54	0.87	4.75
Fe	2.38	1.18	2.93	18.59	14.31	0.94	25.86	20.14	0.84
N	2.47	4.90	9.92	—	—	—	—	—	—
Mn	1.64	0.83	6.80	41.90	32.78	1.21	29.59	23.43	1.52
Si	0.06	0.06	23.77	0.34	0.52	5.95	0.74	1.14	3.57
S	0.05	0.04	21.35	25.36	34.00	0.56	16.30	22.11	0.75

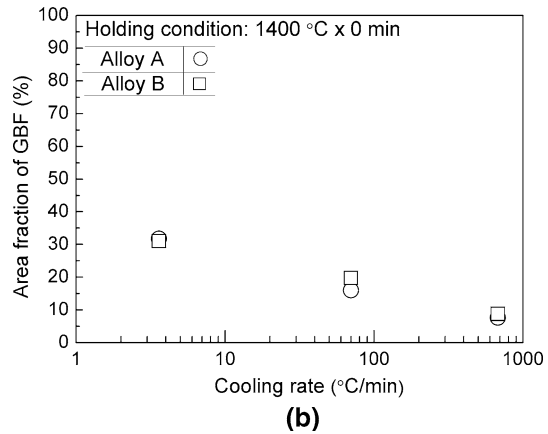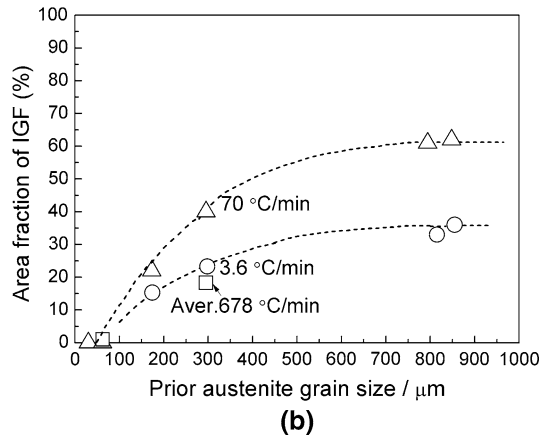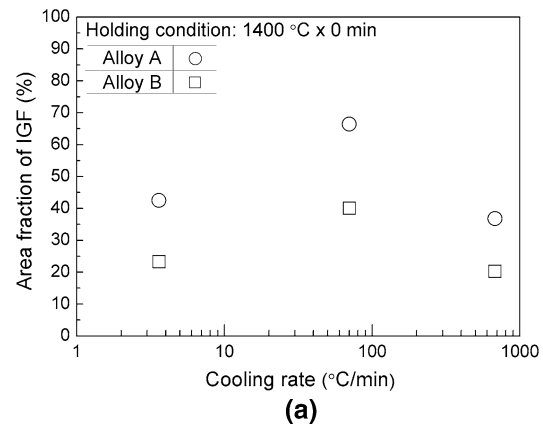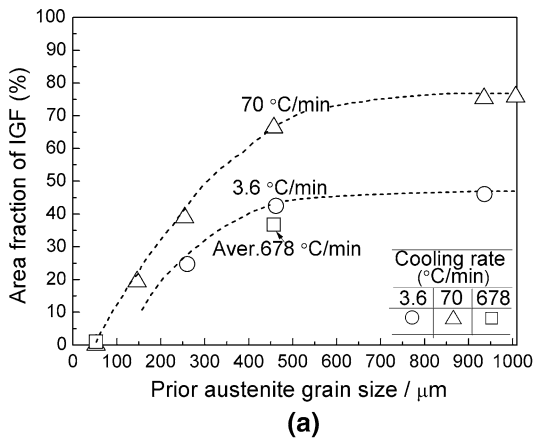*x = O (at. pct)/Ti (at. pct).

(a)

(b)

Fig. 6—Relationship between the prior austenite grain size and the area fraction of IGF (*a*) alloy A; (*b*) alloy B.

(a)

(b)

Fig. 7—Effect of cooling rate on the area fraction of (*a*) IGF and (*b*) GBF [holding at 1673 K (1400 °C) × 0 min].

density. Fine-grained austenite contains a high density of grain boundaries, which are the primary nucleation sites for GBF, and this gives high probability of GBF formation occurring at low undercooling ($\Delta T = \mathrm{Ae}_3\text{-}T_s$), *i.e.*, the high temperature product.[57]

C. Effect of Cooling Rate on the IGF Formation

In the present work, the cooling rate of 3.6 °C/min is close to the actual cooling rate of the CGHAZ in weldments,[58] and, moreover, the cooling rates of 70 and 678 °C/min were used to study if the fraction of IGF could be increased with increasing cooling rate. Figure 7 shows that the fraction of IGF increases and that of GBF decreases with increasing cooling rate from 3.6 to 70 °C/min. The reason for the difference with respect to the cooling rate is that the starting temperature of the GBF formation is higher than that of the IGF formation and since the growth time of GBF is much longer at a cooling rate of 3.6 °C/min compared to a cooling rate of 70 °C/min, the formation of IGF is suppressed for a cooling rate of 3.6 °C/min, since there is less physical space left inside the grains.[55] Moreover, both the fraction of IGF and that of GBF decrease with increasing cooling rate from 70 to 678 °C/min, since the formation of bainite and martensite will occur in the

lower temperature range, according to the CCT diagram for similar steels.[59] In summary, 70 °C/min is the most suitable cooling rate to use among the cooling rates used in this work.

Figures 12 and 13 show EBSD band contrast and inverse pole figure (IPF) colored images of the microstructures. In the steels which were cooled at a rate of 3.6 °C/min, the microstructure in the IPF map is coarse IGF and pearlite. This microstructure has already been identified by a combination of differential scanning calorimetry (DSC) and metallographic examinations for the same alloy, cooled at the same condition.[60] In the steels which were cooled using a rate of 70 °C/min, it is found that the acicular units of IGF have different orientations with the neighboring bainite units in the IPF map. The parallel bainite laths in individual packets have almost the same orientation and the microstructure is similar to the one reported by Wan *et al.*[10] In the steels which were cooled at a rate of 678 °C/min, the interlocked IGF microstructure also exists. However, the fraction of IGF is much lower than in the specimens which were cooled at a rate of 70 °C/min. To validate the EBSD observations, the area fraction of IGF was compared with the CLSM results and they were in good agreement. In the IPF map of alloy B cooled at an average rate of 678 °C/min, it is found that the prior austenite grain is subdivided into several blocks, which is typical for lath martensite in low-carbon
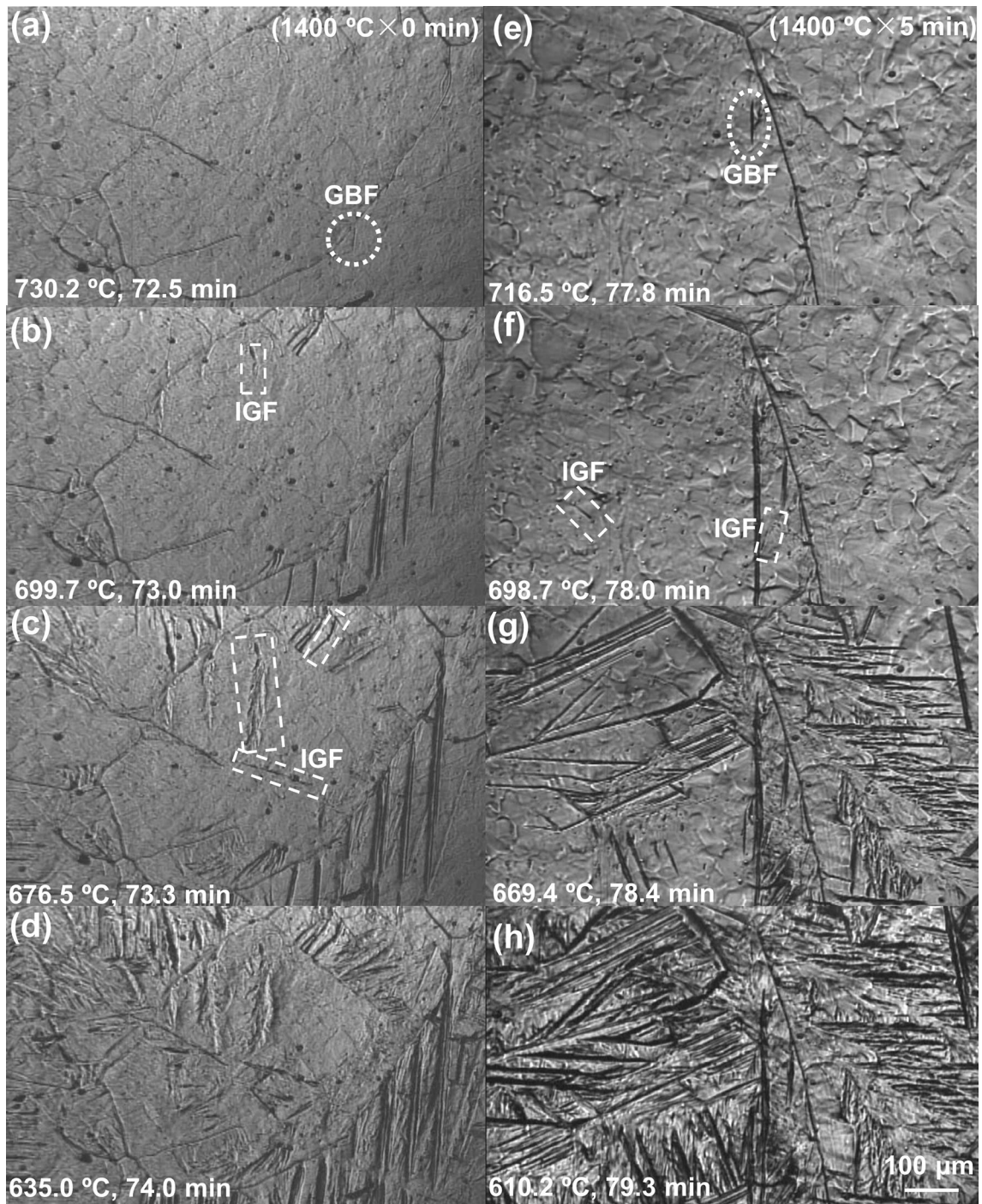
Fig. 8—Typical CLSM images of IGF formation in alloy A. (*a*) holding at 1673 K (1400 °C) × 0 min; (*b*) holding at 1673 K (1400 °C) × 5 min.

alloys.[61–63] However, much larger size units with the same crystal orientation are found in the IPF map of alloy A cooled at an average rate of 678 °C/min. This microstructure is most probably due to a larger grain size in this steel sample, since it is known that the martensite unit size depends on parent austenite grain size.[64,65] The matrix is most likely a mixture of martensite and bainite, and since their structures are similar,[66,67] no attempt was

made to try to separate them. It is also known that bainite can grow below the starting temperature of martensite (M_s),[68] and hence it may even be difficult to separate them based on dynamic studies.

The morphology of the IGF phase changes from a coarse microstructure into a fine microstructure (acicular shape IGF) when the cooling rate increases. However, the fraction of IGF is quite small in the case of a
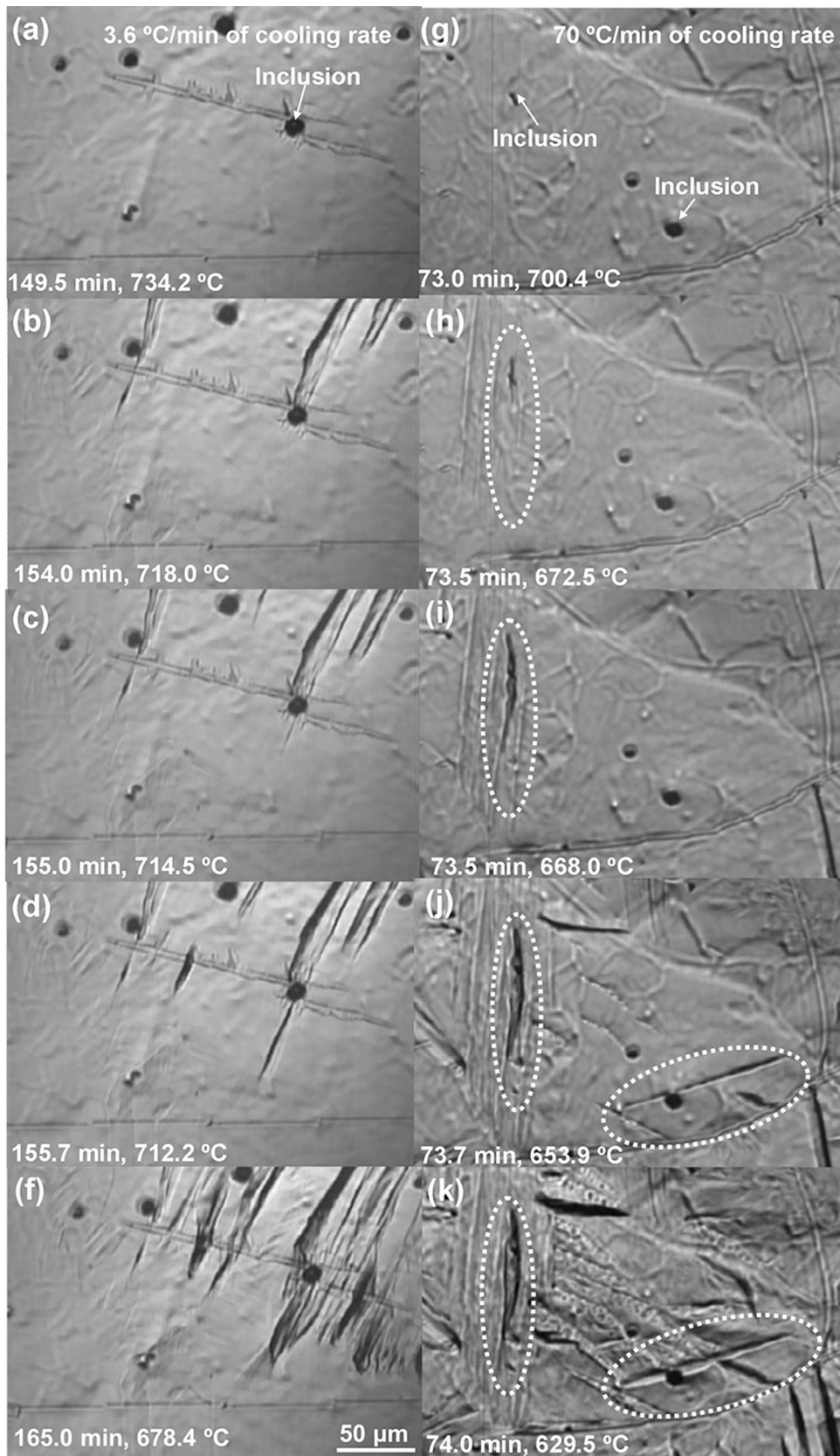
Fig. 9—Typical CLSM images for IGF formation in alloy A, held at 1673 K (1400 °C). (*a*) through (*f*) cooling rate of 3.6 °C/min, and (*g*) through (*k*) cooling rate of 70 °C/min from 1223 K to 673 K (950 °C to 400 °C).
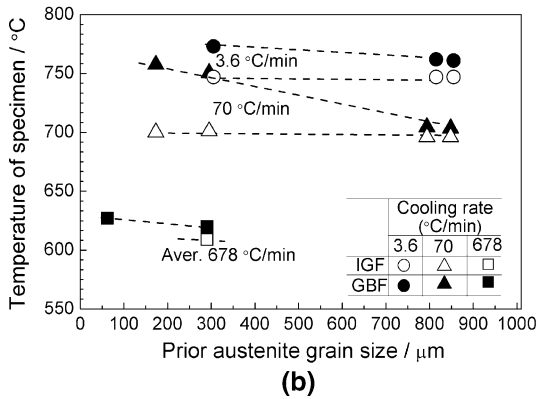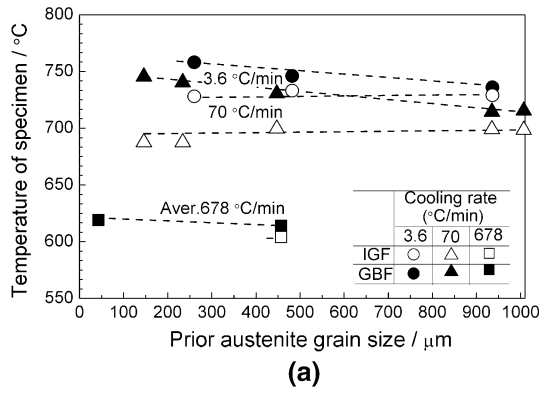
Fig. 10—Effect of prior austenite grain size and cooling rate on the starting temperature of IGF and GBF formation. (*a*) alloy A, (*b*) alloy B.

cooling rate of 678 °C/min. Thus, in order to obtain the desired microstructure of fine IGF units with a large phase fraction, an intermediate cooling rate of 70 °C/min is the most suitable one for the investigated alloys in the present work.

Figure 10 shows that the values of $T_{GBF,s}$ and $T_{IGF,s}$ decrease with increasing cooling rate. The values of $T_{GBF,s}$ and $T_{IGF,s}$ for alloy A and B held at 1673 K (1400 °C) × 0 minutes were selected to determine a schematic CCT diagram, see Figure 14. It is here found that $T_{GBF,s}$ is higher than $T_{IGF,s}$ at each cooling condition, which is expected since the grain boundaries should be the primary nucleation sites and the inclusions should be the secondary nucleation sites.[57] Furthermore, the relationship between the driving force of ferrite formation (ΔG_m and ΔG_v) and the starting temperatures of ferrite formation ($T_{GBF,s}$ and $T_{IGF,s}$) was calculated using Thermo-Calc[27] and the TCFE7 database[28], and the results are shown in Figure 15. The calculated value of ΔG_m at about 973 K (700 °C) is in agreement with a previous study,[54] and it can be noted that the driving force for ferrite formation increases with increasing cooling rate.
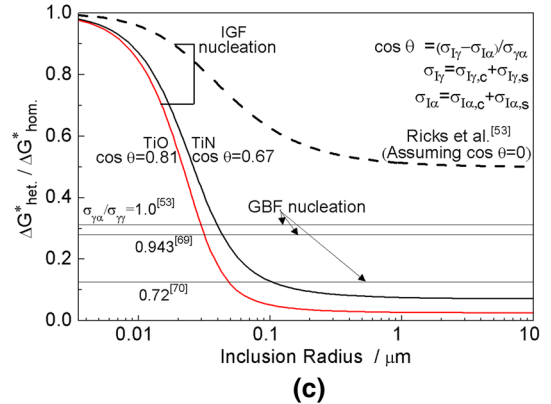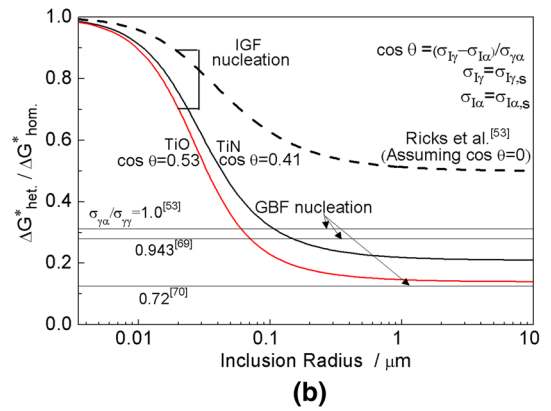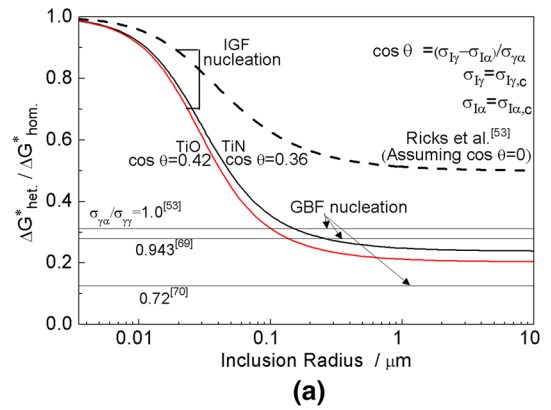

Fig. 11—Effect of inclusion radius on energy barrier to heterogeneous nucleation to ferrite at inclusions, $\Delta G_{het.}^{*}$, normalized with respect to homogeneous nucleation barrier, $\Delta G_{hom.}^{*}$. (*a*) Chemical interfacial energy is used for the calculation; (*b*) Misfit strain energy is used for the calculation; (*c*) Chemical energy and misfit strain energy are used for the calculation.

The driving force, ΔG_v, at different temperatures was used to calculate the normalized energy barrier, $\Delta G_{het.}^{*}/\Delta G_{hom.}^{*}$, of IGF and GBF nucleation, based on the methods from Eqs. [1] through [14]. The calculation results for the energy barrier of IGF nucleation on TiO
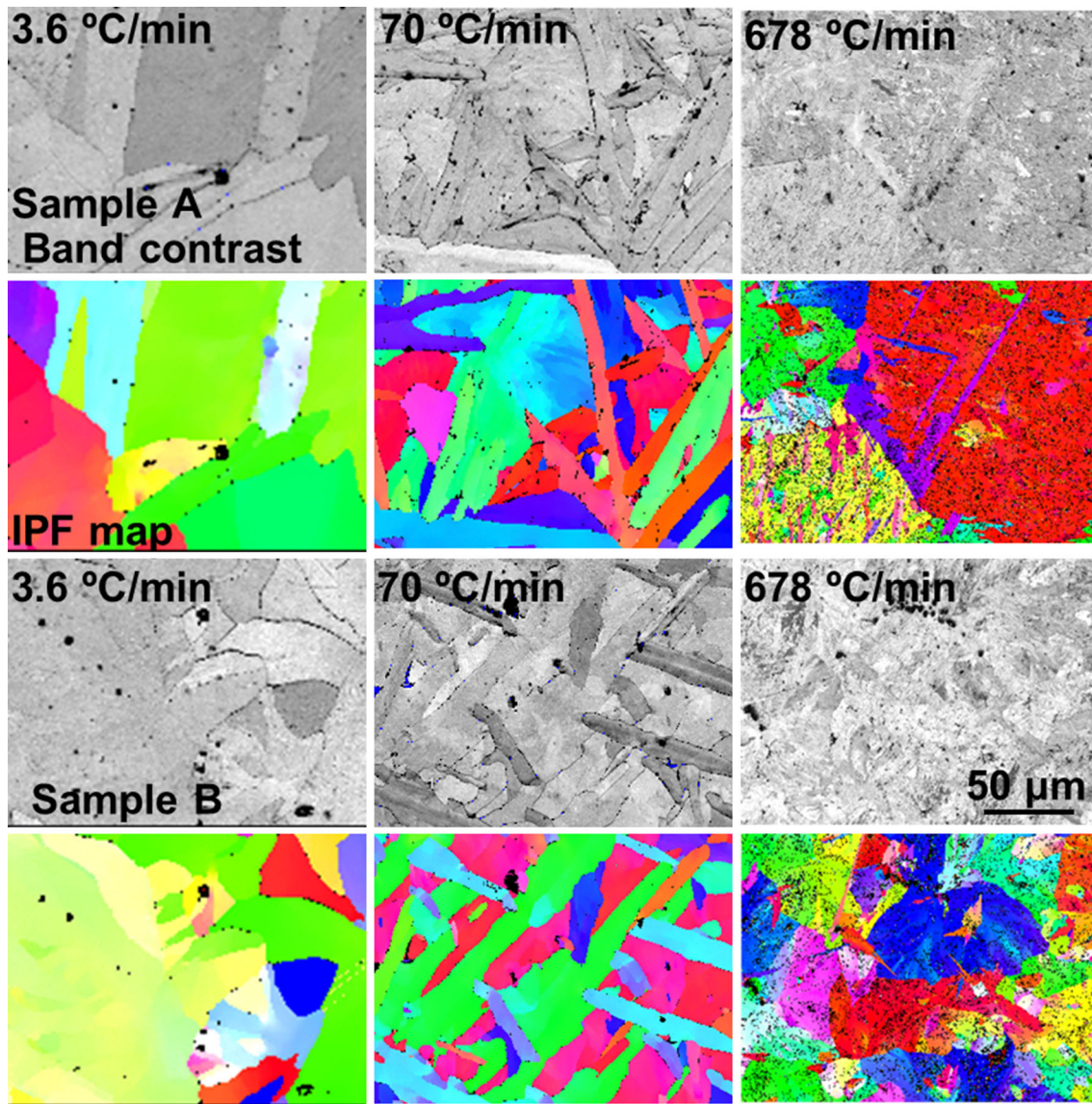
Fig. 12—EBSD analysis of alloy A and alloy B at different cooling rates (step size 0.8 μm).

and TiN is shown in Figures 16(a) and (b). It can be seen that when the inclusion size is fixed, the normalized energy barrier $\left(\Delta G^*_{\text{het.}}/\Delta G^*_{\text{hom.}}\right)$ decreases with decreasing temperature from 1073 K to 873 K (800 °C to 600 °C). Thus, there is a higher potency for IGF nucleation from inclusion surface at a lower temperature. Furthermore, the calculation results in Figure 16 could explain why the IGF fraction at the intermediate cooling rate of 70 °C/min is higher than at a slow cooling rate of 3.6 °C/min.

V. CONCLUSIONS

1. The inclusions in the steel with Ti_2O_3 addition (alloy A) are TiO_x + MnS inclusions and in the steel with TiN addition (alloy B) the inclusions are identified as TiN + MnS + Mn-Al-Si-Ti-O inclusion. Preferred nucleation of intragranular ferrite (IGF) was found to occur from the TiO_x and TiN phases and the fraction of IGF was larger in the steel with Ti_2O_3 addition compared to the steel with TiN addition. The reason for this difference is that the TiO_x phase
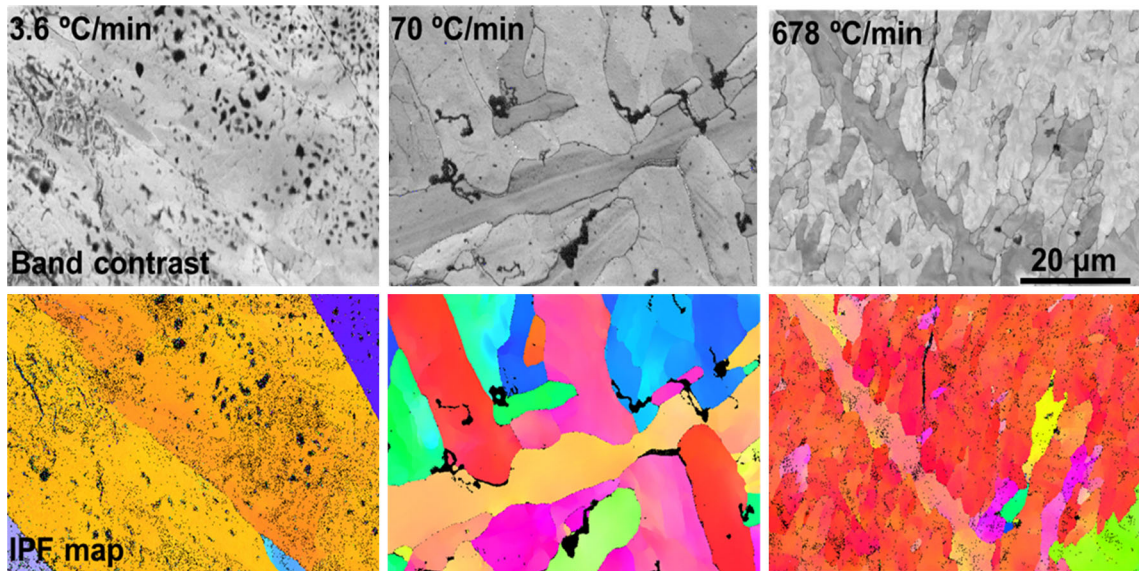
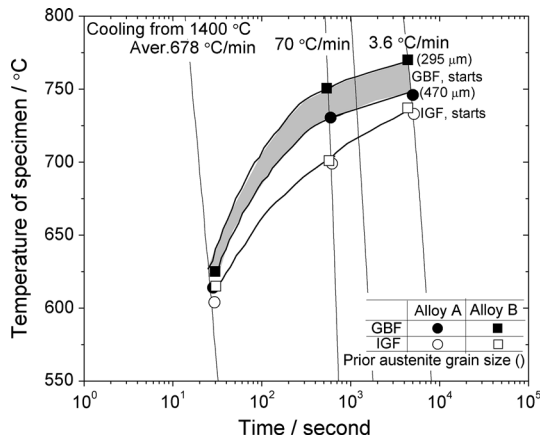Fig. 13—EBSD analysis of alloy A for different cooling rates (step size 0.1 μm).

Fig. 14—Schematic CCT diagram for starting temperature of GBF and IGF formation in alloy A and alloy B.
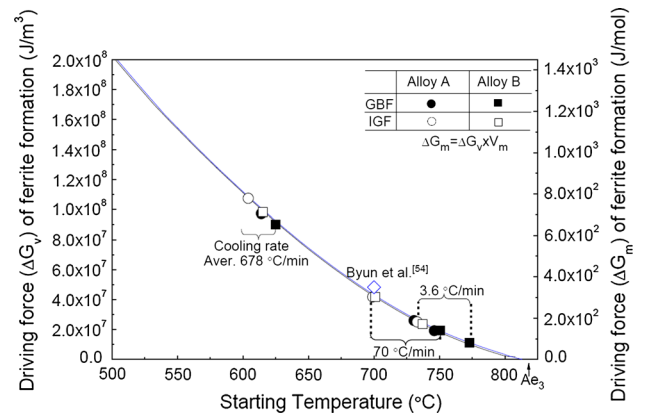

Fig. 15—Relationship between the driving force and the starting temperature of the ferrite formation.

provides more potent nucleation sites for IGF than the TiN phase.

2. The fraction of IGF in the steels which was cooled using a rate of 70 °C/min was larger than the steels which were cooled either more rapidly or slower. The reason is the competition with grain boundary ferrite (GBF) for slower cooling and the competition with martensite and bainite for faster cooling. Further-

more, it should be noted that IGF is refined and the starting temperatures of IGF and GBF decrease with increasing cooling rate.

3. The IGF fraction increases with increasing prior austenite grain size, and the starting temperature of GBF formation is higher for the steel containing a smaller grain size. However, the starting temperature of IGF formation is independent of the grain size.
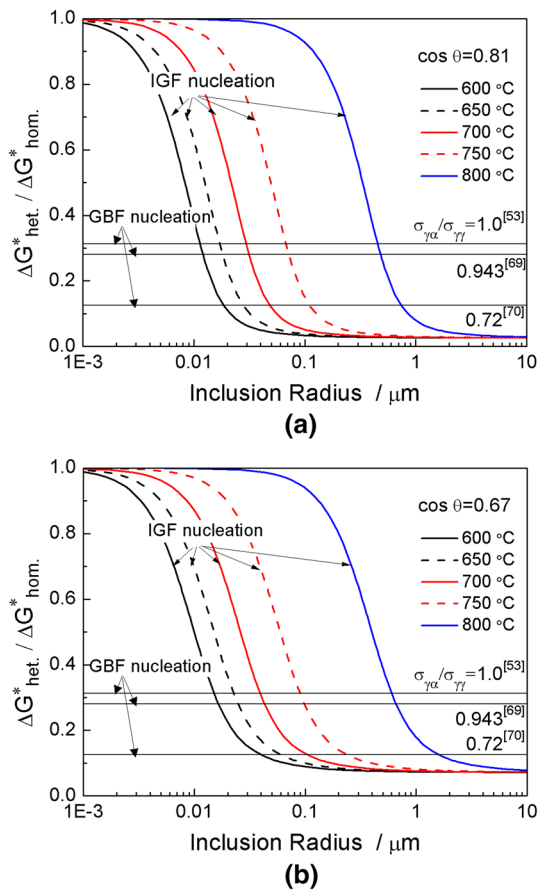
(a)

(b)

Fig. 16—Effect of temperature on the normalized energy barrier for the nucleation of IGF and GBF. (*a*) TiO nucleation site; (*b*) TiN nucleation site.

REFERENCES

1. J. Takamura and S. Mizoguchi: *Proc. 6th Int. Iron and Steel Cong*, ISIJ, Nagoya, 1990, vol. 1, pp. 591–97.
2. O. Wijk: *Proc. 7th Int. Conf. Refining Process* (*SCANINJECT VII*), Luleå, Sweden, 1995, pp. 35–67.
3. Ø. Grong, L. Kolbeinsen, C. van der Eijk, and G. Tranell: *ISIJ Int.*, 2006, vol. 46, pp. 824–31.
4. M. Kiviö and L. Holappa: *Metall. Mater. Trans. B*, 2012, vol. 43B, pp. 233–40.
5. W. Mu, P.G. Jönsson, and K. Nakajima: *ISIJ Int.*, 2014, vol. 54, pp. 2907–16.
6. W. Mu, P.G. Jönsson, H. Shibata, and K. Nakajima: *Steel Res. Int.*, 2015, , DOI:10.1002/srin.201500061.
7. H. Terasaki, T. Yamada, and Y. Komizo: *Mater. Sci. Forum*, 2008, vols. 580–582, pp. 33–36.
8. W. Bin and S. Bo: *Steel Res. Int.*, 2012, vol. 83, pp. 487–95.
9. B. Wen and B. Song: *Ninth International Conference on Molten Slags, Fluxes and Salts* (*Molten 12*), Beijing, 2012, p. 160.
10. X. Wan, K. Wu, G. Huang, and R. Wei: *Steel Res. Int.*, 2014, vol. 85, pp. 243–50.
11. D. Zhang, H. Terasaki, and Y. Komizo: *Acta Mater.*, 2010, vol. 58, pp. 1369–78.
12. D. Zhang, Y. Shintaku, S. Suzuki, and Y. Komizo: *Metall. Mater. Trans. A*, 2012, vol. 43A, pp. 447–58.
13. N. Kikuchi, S. Nabeshima, Y. Kishimoto, Y. Ishiguro, and S. Sridhar: *ISIJ Int.*, 2009, vol. 49, pp. 1036–45.
14. T. Yamada, H. Terasaki, and Y. Komizo: *Weld. Int.*, 2009, vol. 23, pp. 376–81.
15. A.O. Kluken, Ø. Grong, and J. Hjelen: *Metall. Mater. Trans. A*, 1991, vol. 22A, pp. 657–63.
16. C. van der Eijk, Ø. Grong, and J. Hjelen: in *Proc. Int. Conf. on Solid-solid Phase Trans.'99* (*JIMIC-3*), M. Koiwa, K. Otsuka, and T. Miyazaki, eds., JIM, Sendai, 1999, pp. 1573–76.
17. X.L. Wan, H.H. Wang, L. Cheng, and K.M. Wu: *Mater. Charact.*, 2012, vol. 67, pp. 41–51.
18. L. Cheng and K.M. Wu: *Acta Mater.*, 2009, vol. 57, pp. 3754–62.
19. D. Phelan and R. Dippenaar: *Metall. Mater. Trans. A*, 2004, vol. 35A, pp. 3701–06.
20. A. Phelan, N. Stanford, and R. Dippenaar: *Mater. Sci. Eng. A*, 2005, vol. 407, pp. 127–34.
21. H. Chikama, H. Shibata, T. Emi, and M. Suzuki: *Mater. Trans. JIM*, 1996, vol. 37, pp. 620–26.
22. H. Shibata, H.B. Yin, S. Yoshinaga, T. Emi, and M. Suzuki: *ISIJ Int.*, 1998, vol. 38, pp. 149–56.
23. K. Nakajima and S. Mizoguchi: *Metall. Mater. Trans. B*, 2001, vol. 32B, pp. 629–41.
24. Q. Liu, H. Shibata, P. Hedström, P. Jönsson, and K. Nakajima: *ISIJ Int.*, 2013, vol. 53, pp. 1237–44.
25. J. Janis, R. Inoue, A. Karasev, K. Nakajima, and P.G. Jönsson: *Steel Res. Int.*, 2009, vol. 80, pp. 450–56.
26. K.F. Kelton and A.L. Greer: *Nucleation in Condensed Matter—Application in Materials and Biology*, Elsevier, Oxford, 2010, pp. 165–226.
27. J.-O. Andersson, T. Helander, L. Höglund, P. Shi, and B. Sundman: *CALPHAD*, 2002, vol. 26, pp. 273–312.
28. TCS Steels/Fe-Alloys Database Version 7.0, Thermo-Calc Software AB, Sweden, 2012.
29. T. Furuhara: *Tetsu-to-Hagané*, 2003, vol. 89, pp. 497–509.
30. Z.-G. Yang and M. Enomoto: *Mater. Sci. Eng. A*, 2002, vol. 332, pp. 184–92.
31. Z.-G. Yang and M. Enomoto: *Metall. Mater. Trans. A*, 2001, vol. 32A, pp. 267–74.
32. M. Enomoto: *Metal. Mater.*, 1998, vol. 4, pp. 115–23.
33. Z.-G. Yang, C. Zhang, and T. Pan: *Mater. Sci. Forum*, 2005, vols. 475–479, pp. 113–16.
34. J.H. van der Merwe: *J. Appl. Phys.*, 1963, vol. 34, pp. 117–22.
35. N. Pan, B. Song, Q. Zhai, and B. Wen: *J. Chin Rare Earth Soc.*, 2010, vol. 28, pp. 126–30.
36. A.R. Mills, G. Thewlis, and J.A. Whiteman: *Mater. Sci. Technol.*, 1987, vol. 3, pp. 1051–61.
37. F.S. Galasso: *Structure and properties of inorganic solids*, 1st ed., Pergamon Press Ltd., Headington Hill Hall, Oxford, 1970, pp. 28–31.
38. S. Zhang, N. Hattori, M. Enomoto, and T. Tarui: *ISIJ Int.*, 1996, vol. 36, pp. 1301–09.
39. Y.O. Ciftci, Y. Ünlü, K. Colakoglu, and E. Deligoz: *Phys. Scr.*, 2009, vol. 80, pp. 1–6.
40. M. Fukuhara and A. Sanpei: *ISIJ Int.*, 1993, vol. 33, pp. 508–12.
41. A.J. Perry: *Thin Solid Films*, 1990, vols. 193–194, pp. 463–71.
42. J.M. Howe: *Interfaces in Materials*, Wiley, New York, 1997, p. 378.
43. D.A. Porter and K.E. Easterling: *Phase Formation in Metals and Alloys*, 2nd ed., Chapman & Hall, Boundary Row, London, 1992, pp. 263–75.
44. D. Kim, K. Han, B. Lee, I. Han, J.H. Park, and C. Lee: *Metall. Mater. Trans. A*, 2014, vol. 45A, pp. 2046–54.

45. H. Homma, S. Ohkita, S. Matsuda, and K. Yamamoto: *Weld. J.*, 1987, vol. 66, pp. 301.s–09.s.
46. J.-L. Lee and Y.-T. Pan: *Mater. Sci. Technol.*, 1992, vol. 8, pp. 236–44.
47. J.-L. Lee and Y.-T. Pan: *Metall. Trans. A*, 1993, vol. 24A, pp. 1399–408.
48. J.-L. Lee: *Acta Metall. Mater.*, 1994, vol. 42, pp. 3291–98.
49. J.M. Gregg and H.K.D.H. Bhadeshia: *Acta Mater.*, 1997, vol. 43, pp. 739–48.
50. J.M. Gregg and H.K.D.H. Bhadeshia: *Metal. Mater. Trans. A*, 1994, vol. 25A, pp. 1603–11.
51. A. Takada, Y. Komizo, H. Terasaki, T. Yokota, K. Oi, and K. Yasuda: *Weld. Int.*, 2015, vol. 29, pp. 254–61.
52. Ø. Grong, A.O. Kluken, H.K. Nylund, A.L. Dons, and J. Hjelen: *Metal. Mater. Trans. A*, 1995, vol. 26A, pp. 525–34.
53. R. Ricks, P.R. Howell, and G.S. Barritte: *J. Mater. Sci.*, 1982, vol. 17, pp. 732–40.
54. J.-S. Byun, J.-H. Shim, Y.W. Cho, and D.N. Lee: *Acta Mater.*, 2003, vol. 51, pp. 1593–606.
55. S Liu and DL Olson: *Weld. J.*, 1986, vol. 65, pp. 139.s–49.s.
56. Y. Tomita, N. Saito, T. Tsuzuki, Y. Tokunaga, and K. Okamoto: *ISIJ Int.*, 1994, vol. 34, pp. 829–35.
57. P. Harrison and R. Farrar: *Metal Constr.*, 1987, vol. 19, pp. 392–99.
58. N. Mori, H. Homma, S. Okita, M. Wakabayashi: *Mechanism of notch toughness improvement in Ti-B bearing welds metals*, IIW Doc. IX-1196-81, International Institute of Welding, 1981, pp. 1–16.
59. A.S. Podder, A.S. Pandit, A. Murugaiyan, D. Bhattacharjee, and R.K. Ray: *Ironmak. Steelmak.*, 2007, vol. 34, pp. 83–88.
60. W. Mu, H. Shibata, P. Hedström, P.G. Jönsson, and K. Nakajima: *Steel Res. Int.*, 2016, vol. 87, pp. 10–16.
61. S. Morito, H. Tanaka, R. Konishi, T. Furuhara, and T. Maki: *Acta Mater.*, 2003, vol. 51, pp. 1789–99.
62. H. Kitahara, R. Ueji, N. Tsuji, and Y. Minamino: *Acta Mater.*, 2006, vol. 54, pp. 1279–88.
63. Z. Hou, P. Hedström, Y. Xu, D. Wu, and J. Odqvist: *ISIJ Int.*, 2014, vol. 54, pp. 2649–56.
64. T. Maki, K. Tsuzaki, and I. Tamura: *Trans. Iron Steel Inst. Jpn.*, 1980, vol. 20, pp. 207–14.
65. S. Morito, H. Saito, T. Ogawa, T. Furuhara, and T. Maki: *ISIJ Int.*, 2005, vol. 45, pp. 91–94.
66. H. Terasaki and Y. Komizo: *Metall. Mater. Trans. A*, 2013, vol. 44A, pp. 2683–89.
67. T. Song and B.C. de Cooman: *Metall. Mater. Trans. A*, 2013, vol. 44A, pp. 1686–705.
68. P. Kolmskog, A. Borgenstam, M. Hillert, P. Hedström, S.S. Babu, H. Terasaki, and Y. Komizo: *Metall. Mater. Trans. A*, 2012, vol. 43A, pp. 4984–88.
69. N.A. Gjostein, H.A. Domian, H.I. Aaronson, and E. Eichen: *Acta Mater.*, 1966, vol. 14, pp. 1637–44.
70. L.H. Van Vlack: *Trans AIME*, 1951, vol. 191, pp. 251–59.